Meteorology and Atmospheric Physics manuscript No.
(will be inserted by the editor)

A coupled mesoscale-model Fourier-method for idealized mountain-wave simulations over Hawaii

John Lindeman · Dave Broutman · Stephen D. Eckermann · Jun Ma · Zafer Boybeyi

Received: soon / Accepted: TBD

Abstract Mesoscale model simulations of representative trade winds impinging upon the Big Island of Hawaii are diagnosed for their mountain wave

J. Lindeman

College of Science, George Mason University, 4400 University Drive, Fairfax, VA 22030, USA.

Tel.: (703) 993-1560

Fax: (703) 993-9280

E-mail: jlindema@gmu.edu

D. Broutman

Computational Physics, Inc., Springfield, VA, USA

S. D. Eckermann

Space Science Division, Naval Research Laboratory, Washington, DC, USA

J. Ma

Computational Physics, Inc., Springfield, VA, USA

Z. Boybeyi

College of Science, George Mason University, Fairfax, VA, USA

Report Documentation Page

Form Approved
OMB No. 0704-0188

Public reporting burden for the collection of information is estimated to average 1 hour per response, including the time for reviewing instructions, searching existing data sources, gathering and maintaining the data needed, and completing and reviewing the collection of information. Send comments regarding this burden estimate or any other aspect of this collection of information, including suggestions for reducing this burden, to Washington Headquarters Services, Directorate for Information Operations and Reports, 1215 Jefferson Davis Highway, Suite 1204, Arlington VA 22202-4302. Respondents should be aware that notwithstanding any other provision of law, no person shall be subject to a penalty for failing to comply with a collection of information if it does not display a currently valid OMB control number.

1. REPORT DATE	2. REPORT TYPE	3. DATES COVERED
2010		**00-00-2010 to 00-00-2010**

4. TITLE AND SUBTITLE	5a. CONTRACT NUMBER
A coupled mesoscale-model Fourier-method for idealized mountain-wave simulations over Hawaii	5b. GRANT NUMBER
	5c. PROGRAM ELEMENT NUMBER
6. AUTHOR(S)	5d. PROJECT NUMBER
	5e. TASK NUMBER
	5f. WORK UNIT NUMBER
7. PERFORMING ORGANIZATION NAME(S) AND ADDRESS(ES) **Naval Research Laboratory,Space Science Division,Washington,DC,20375**	8. PERFORMING ORGANIZATION REPORT NUMBER
9. SPONSORING/MONITORING AGENCY NAME(S) AND ADDRESS(ES)	10. SPONSOR/MONITOR'S ACRONYM(S)
	11. SPONSOR/MONITOR'S REPORT NUMBER(S)

12. DISTRIBUTION/AVAILABILITY STATEMENT
Approved for public release; distribution unlimited

13. SUPPLEMENTARY NOTES
Meteorology and Atmospheric Physics (in press)

14. ABSTRACT
Mesoscale model simulations of representative trade winds impinging upon the Big Island of Hawaii are diagnosed for their mountain wave characteristics by coupling a mesoscale model to a Fourier method. Localized phase-averaged wave momentum fluxes are calculated, which facilitates the study of wave generation from fine-scale topographic features. We find that the wave momentum fluxes are dominated by forcing from subsidiary topographic peaks, with the broader island topography controlling flow splitting and lee vortex generation. Waves also arise at the far northern and southern extremities of the island by acceleration of split flow. The strength of the local momentum fluxes prove to be sensitive to a small change in the incident flow direction. Areally integrated fluxes (wave drag) align closely with the incident flow direction, and are an order of magnitude smaller than linear predictions and an order of magnitude larger than corresponding dividing streamline predictions. We briefly discuss the relevance of these results to the parameterization of subgrid-scale mountain wave drag in climate and weather models.

15. SUBJECT TERMS

16. SECURITY CLASSIFICATION OF:			17. LIMITATION OF ABSTRACT	18. NUMBER OF PAGES	19a. NAME OF RESPONSIBLE PERSON
a. REPORT	b. ABSTRACT	c. THIS PAGE			
unclassified	**unclassified**	**unclassified**	**Same as Report (SAR)**	**31**	

characteristics by coupling a mesoscale model to a Fourier method. Localized phase-averaged wave momentum fluxes are calculated, which facilitates the study of wave generation from fine-scale topographic features. We find that the wave momentum fluxes are dominated by forcing from subsidiary topographic peaks, with the broader island topography controlling flow splitting and lee vortex generation. Waves also arise at the far northern and southern extremities of the island by acceleration of split flow. The strength of the local momentum fluxes prove to be sensitive to a small change in the incident flow direction. Areally integrated fluxes (wave drag) align closely with the incident flow direction, and are an order of magnitude smaller than linear predictions and an order of magnitude larger than corresponding dividing streamline predictions. We briefly discuss the relevance of these results to the parameterization of subgrid-scale mountain wave drag in climate and weather models.

Keywords mountain waves · drag · momentum fluxes

1 Introduction

Observational and numerical studies have shown that mountain wave generation can be affected by low-level nonlinear processes such as flow stagnation on the upwind slope and subsequent flow splitting around the mountain (Smith, 1989; Smolarkiewicz and Rotunno, 1989, 1990; Miranda and James, 1992; Schär and Durran, 1997; Smith et al, 2002; Jiang et al, 2005; Smith et al, 2007; Wells et al, 2008a; Eckermann et al, 2010). As Smith et al (2007) note

in their overview of mountain waves observed over the Pyrenees during the Mesoscale Alpine Project, "...any quantitative prediction of mountain wave generation must take full account of these lower troposphere processes."

A mesoscale meteorological model can account for a range of nonlinear processes. Still there is good reason to involve a linear Fourier method in the simulation and analysis of mountain waves wherever the wavefield is quasi-linear. Fourier methods have great interpretive power and can characterize the properties of waves radiated from nonlinear flow over multiscale orography in ways that simpler analyses of mesoscale model fields cannot, a property utilized here. In this paper, we couple a mesoscale model to a Fourier method, using the mesoscale model to simulate the low-level nonlinear flow and to predict the emerging wavefield, and the Fourier method to simulate the wavefield at altitudes above the nonlinear flow. Our main aim is to understand how momentum flux is generated by the individual peaks and orographic features of Hawaii.

The present method debuted in Lindeman et al (2008), for idealized topography and a uniform background wind and stratification (see also Eckermann et al, 2010). Here we consider realistic topography but leave the background uniform. We examine mountain waves generated by the Big Island of Hawaii (hereafter referred to as Hawaii), which has four pronounced peaks (Figure 1). Two of the peaks, Mauna Loa and Mauna Kea, are over 4 km in elevation. All four peaks are sufficiently distinct and isolated that possible wave generation from each can be distinguished.

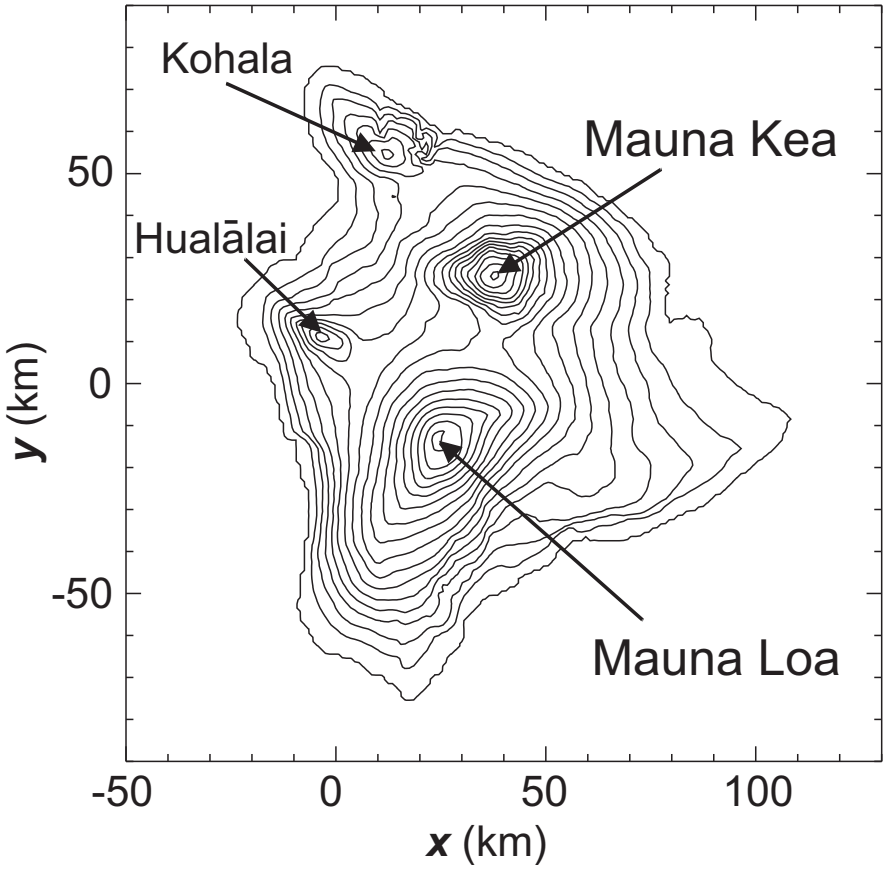

Fig. 1 Topographic elevation $h(x, y)$ for Hawaii (GTOPO30 interpolated to 1×1 km^2 resolution) identifying the four main peaks. The contour interval is 250 m and the peak elevation is 4066 m.

Hawaii's climate is fairly consistent year-round with east-northeasterly trade winds (Rasmussen et al, 1989), and an average Froude number $Fr \approx 0.2$ (Smolarkiewicz et al, 1988). Here $Fr = U/(Nh_m)$, where U is the upstream surface wind speed, N is the buoyancy frequency, and h_m is the height of the tallest peak. Thus blocking and flow separation are expected, as has been confirmed in field experiments and numerical studies (Smolarkiewicz et al, 1988;

Rasmussen et al, 1989; Smith and Grubišić, 1993; Chen and Nash, 1994; Wang et al, 1998; Chen and Feng, 2001; Hafner and Xie, 2003).

In Section 2 we describe the modeling tools used here, namely the mesoscale model, the Fourier method, and a Hilbert transform method for calculating local wave momentum fluxes. In Section 3, we apply these tools to mountain waves generated by representative winds impinging on Hawaii from the east-northeast and from the northeast. We also compare these wave solutions with those from the Fourier method using a linearized lower boundary condition and a dividing streamline approximation. In Section 4, we discuss and summarize the main results of this work.

2 Modeling Tools

2.1 Weather, Research, and Forecasting (WRF) model

For our numerical simulations, we use version 3.1.1 of the Advanced Research WRF (Weather, Research, and Forecasting) model, described in detail by Skamarock et al (2008). The model is nonlinear and fully compressible, discretized with fifth/third-order finite differences for the horizontal/vertical advection, and third-order Runga-Kutta for the time stepping.

In all WRF simulations, the computational domain is 900 km in each horizontal direction (x, y) and 22 km in the vertical direction (z). The gridpoint spacing is 1 km in the horizontal and about 120 m in the vertical. (WRF uses a pressure-based terrain-following vertical coordinate.) Inflow/outflow condi-

tions are applied at the lateral boundaries, and the top of the model is a rigid lid where the vertical velocity is zero. To minimize reflection of upward-propagating gravity waves from this lid, an implicit sponge layer is included at $z = 11$–22 km. In this layer are 58 vertical grid levels, and the damping coefficient varies with height according to eq. (21) of Klemp et al (2008) with a peak damping rate at $z = 22$ km of 0.2 s^{-1}.

In all simulations we use a frictionless (free-slip) lower boundary, a 1.5-order turbulent closure scheme, and omit Coriolis effects and moisture. Each simulation is run out to $t = 12$ hours, which allows sufficient time for the low-level nonlinear response to develop, and for mountain wave fields to propagate through the full vertical domain and attain a quasi-steady state. The lateral boundaries are sufficiently far away from Hawaii as to be unaffected by the low-level nonlinear processes after 12 hours.

The Hawaiian topography was obtained from the United States Geological Survey (USGS) GTOPO30 data base, interpolated linearly onto a 1×1 km^2 Cartesian grid, then smoothed using a two-dimensional five-point running average to suppress forcing of unrealistic gridpoint-scale noise (Davies and Brown, 2001). The four major island peaks in Figure 1 are retained after this smoothing, and the peak elevation (Mauna Loa) is reduced only slightly, from 4066 m to 4000 m.

2.2 The Fourier Transform (FT) Method

The far-field mountain waves generated by WRF are coupled to a Fourier-transform (FT) solution of the form

$$w(x,y,z) = \int_{-\infty}^{\infty}\int \tilde{w}(k,l,z)\; e^{\imath(kx+ly)} dk\, dl\;, \tag{1}$$

where w is the vertical velocity, $\tilde{w}(k,l,z)$ is the vertical eigenfunction, and k,l are the horizontal wavenumber components. For a nonuniform background, $\tilde{w}(k,l,z)$ can be approximated with ray theory, as in the Jan Mayen trapped wave simulations of Eckermann et al (2006). For a uniform background, and in the anelastic approximation, the vertical eigenfunctions are simply

$$\tilde{w}(k,l,z) = \left[\frac{\rho(z_i)}{\rho(z)}\right]^{1/2} \tilde{w}(k,l,z_i) e^{\imath m(z-z_i)}, \tag{2}$$

where z_i is an initialization height, and the vertical wavenumber m follows from the dispersion relation

$$m = -(k^2+l^2)^{1/2}\left(\frac{N^2}{\hat{\omega}^2}-1\right)^{1/2}. \tag{3}$$

The background density is ρ, and the buoyancy frequency is N. Since we assume stationary waves, the intrinsic frequency is $\hat{\omega} = -kU - lV$, where $\mathbf{U} \equiv (U,V)$ is the background horizontal wind vector. Additional terms in the dispersion relation can be included (e.g. anelastic terms) but are omitted here since they have minor effects. Trapping and tunneling effects (Broutman et al, 2006, 2009) can also be omitted from the formulation in this application due to the uniform background, while evanescent modes ($\hat{\omega}^2 > N^2$) are omitted for simplicity since our focus is on the propagating wave components.

For linear problems ($Fr \gg 1$) the FT method can be initialized at the surface ($z_i = 0$) using the topographic elevation $h(x, y)$ to yield the lower boundary condition

$$\tilde{w}(k, l, z_i = 0) = -\imath\hat{\omega}\tilde{h}(k, l), \tag{4}$$

where $\tilde{h}(k, l)$ is the Fourier transform of $h(x, y)$. Eqs. (1)-(3) give the resulting linear steady-state mountain wave response.

For nonlinear problems ($Fr \lesssim 1$), the FT method is initialized by the WRF solution at a height z_i sufficiently above the low-level nonlinearity. That is,

$$\tilde{w}(k, l, z_i) = \tilde{w}_W(k, l, z_i, t_i), \tag{5}$$

where $\tilde{w}_W(k, l, z_i, t_i)$ is the horizontal two-dimensional Fourier transform of the WRF vertical velocity at height z_i and time t_i. The time t_i is chosen to be long enough to approximate the quasi-steady mountain wave response at z_i. After testing we found $z_i = 6$ km and $t_i = 12$ hours to be acceptable choices for this work. As in Lindeman et al. (2008), we ensured that z_i was above all occurrences of turbulent kinetic energy, as calculated by WRF.

2.3 Phase averaged momentum fluxes

The gravity wave polarization relations can be used to compute the horizontal perturbation velocities u, v from the vertical velocity w. The polarization relations are applied in Fourier space, using the form (2) for $\tilde{w}(k, l, z)$ and (3) for the dispersion relation. Since u, v, and w can be obtained as complex functions (see the following paragraph), we can compute the local phase-averaged

momentum fluxes using

$$F_x = \rho\overline{uw} = \frac{\rho}{4}\left(uw^* + u^*w\right) , \tag{6}$$

$$F_y = \rho\overline{vw} = \frac{\rho}{4}\left(vw^* + v^*w\right) , \tag{7}$$

where * indicates a complex conjugate. These localized momentum fluxes are particularly useful in the present context because they can be associated with waves forced by flow across the individual peaks of Hawaii identified in Figure 1, as will be shown in Section 3.

We obtain complex spatial variables in the following way. Consider the vertical velocity $w(x, y, z)$. If w is real, its Fourier transform will obey $\tilde{w}(k, l, z) = \tilde{w}^*(-k, -l, z)$. We first set $\tilde{w}$ to zero for half of the wavenumbers; e.g., those for which the intrinsic frequency $\hat{\omega} = -kU - lV$ is negative. We multiply $\tilde{w}$ by two in order to account for the removal of amplitude information from those wavenumbers and then take the inverse Fourier transform. The result is a complex w. The real part of this complex w is the same as the original w, but an imaginary part has been introduced that is the Hilbert transform (Hahn, 1996) of the original real w. This complex w now represents the original velocity field in complex vector form on the Argand diagram with local peak amplitude w_p and local phase ϕ_w each defined at every point, and similarly for u and v.

This separation of phase and amplitude information allows us to construct locally phase-averaged momentum fluxes, as follows. Eq. (6) is obtained by first multiplying $Re(u) = (u + u^*)/2$ by $Re(w) = (w + w^*)/2$. The component $uw + u^*w^* = 2u_p w_p \cos(\phi_u + \phi_w)$, where ϕ_u and ϕ_w are the local phases of u and

w, respectively. Since from polarization relations $\phi_w = \phi_u \pm \pi$, this component contains a $\cos 2\phi_u$ "beating" term, which is not useful locally and has a zero phase average. By contrast, the other component $uw^* + u^*w = 2u_p w_p \cos(\phi_u - \phi_w) = -2u_p w_p$. Note that phases subtract out of this term. Since $\overline{uw} = -(u_p w_p)/2$, (6) follows, as does (7) from a corresponding expression for $vw^* + v^*w$.

In interpreting F_x and F_y as phase-averaged momentum fluxes, there is an assumption that the spatial wavefield is sufficiently slowly varying that one can meaningfully distinguish a rapidly varying phase from a slowly varying amplitude. The wave field must also be steady and stationary. Those assumptions require formal testing but will be assumed to be valid here. Examples validating the accuracy of these flux relations for waves radiated from linear and nonlinear flow over idealized three-dimensional obstacles are given in Lindeman (2008) and Eckermann et al (2010).

3 Results

Two cases are considered. They are identical except that the background wind direction is from the east-northeast in the first case (Section 3.1) and from the northeast in the second case (Section 3.2). The initial state has constant $N = 0.01$ s^{-1} and a constant mean wind speed of 8 m s^{-1}. For the peak mountain height of $h_m = 4$ km, this gives $Fr = 0.2$.

Using a Sheppard criterion for flow splitting (i.e., $Fr \leq 1$), the dividing streamline height $z_c = h_m(1 - Fr)$ (Snyder et al, 1985). Despite its theoreti-

cal shortcomings (Smith, 1989), this criterion reproduces laboratory measurements of dividing streamlines (e.g., Snyder et al, 1985; Ding et al, 2003), and is commonly used in parameterizations (see Eckermann et al, 2010, and references therein). A simple parameterization of wave activity at $Fr \leq 1$ based on the dividing streamline uses only the topography and flow above z_c to generate mountain waves. For the present value of $Fr = 0.2$, $z_c = 3200\,\mathrm{m}$. Upstream air parcels below z_c are assumed to flow horizontally around Hawaii without contributing to the generation of mountain waves. Thus only the top 800 m of the two tallest Hawaiian peaks generate waves in the dividing streamline approximation. The dividing streamline topography h_{ds} is defined as $h_{ds} = h$ for $z > z_c$ and $h_{ds} = z_c$ otherwise. In the FT method, the dividing streamline initialization is implemented by setting $z_i = z_c$ and $\tilde{w}(k, l, z_i) = -i\hat{\omega}\hat{h}_{ds}$ in (2), where $\hat{h}_{ds}$ is the Fourier transform of h_{ds}.

3.1 Case 1: East-Northeasterly Flow

Figure 2 shows the surface flow from WRF for a background wind of $|\mathbf{U}| = 8\ \mathrm{m\ s^{-1}}$ from the east-northeast, which is a typical direction of surface trade winds impinging upon Hawaii. The streamlines show a primary zone of flow stagnation and splitting along the upslope to Mauna Kea, with this low-level flow diverted around the island. Asymmetric vortices form in the lee of Hawaii in general agreement with previous observations and modeling (Rasmussen et al, 1989; Smith and Grubišić, 1993).

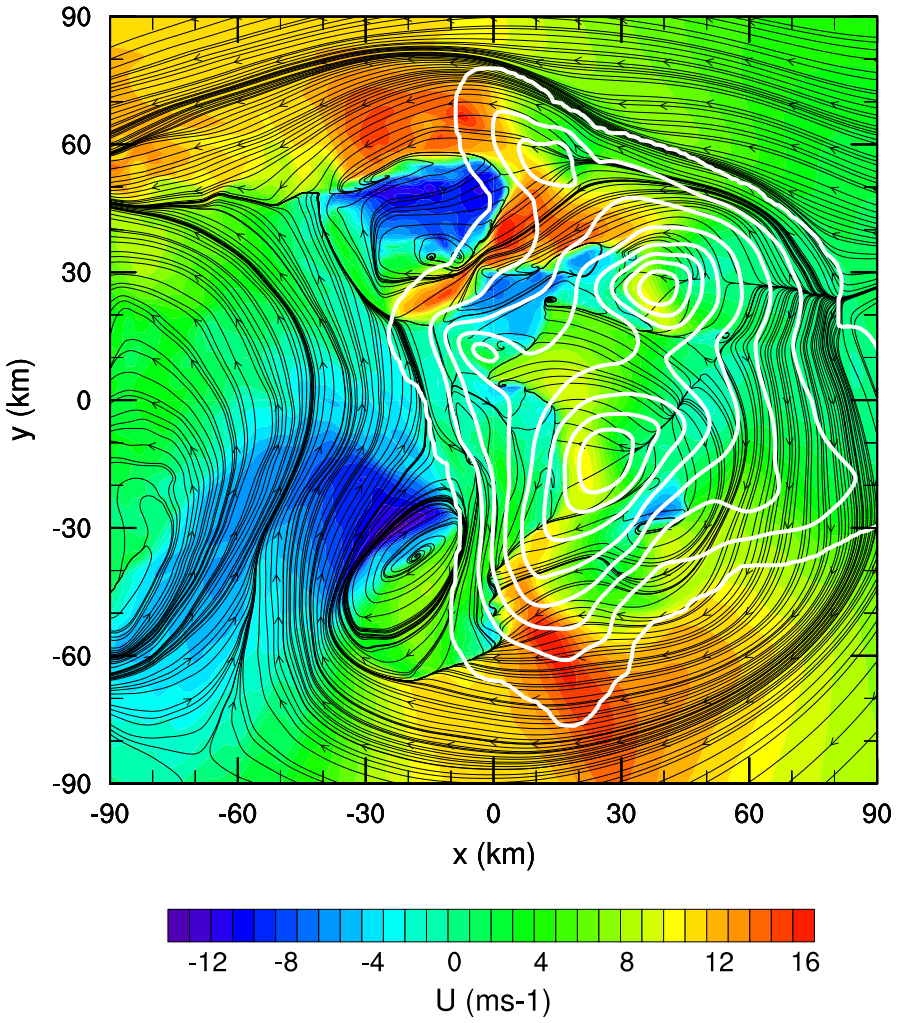

Fig. 2 Case 1. Surface streamlines at $t_i = 12$ hours for the WRF simulation with **U** directed east-northeasterly at 8 m s^{-1}. Color shading shows wind anomalies along the **U** direction (see underlying color bar, units in m s^{-1}). Topography is overlayed as white contours at 500 m intervals.

In the following, the FT solution initialized by WRF (at $z_i = 6\,\mathrm{km}$) will be referred to as the FT/WRF solution. Figure 3 shows the WRF solution (left column) and the FT/WRF solution (right column) for the wave-induced

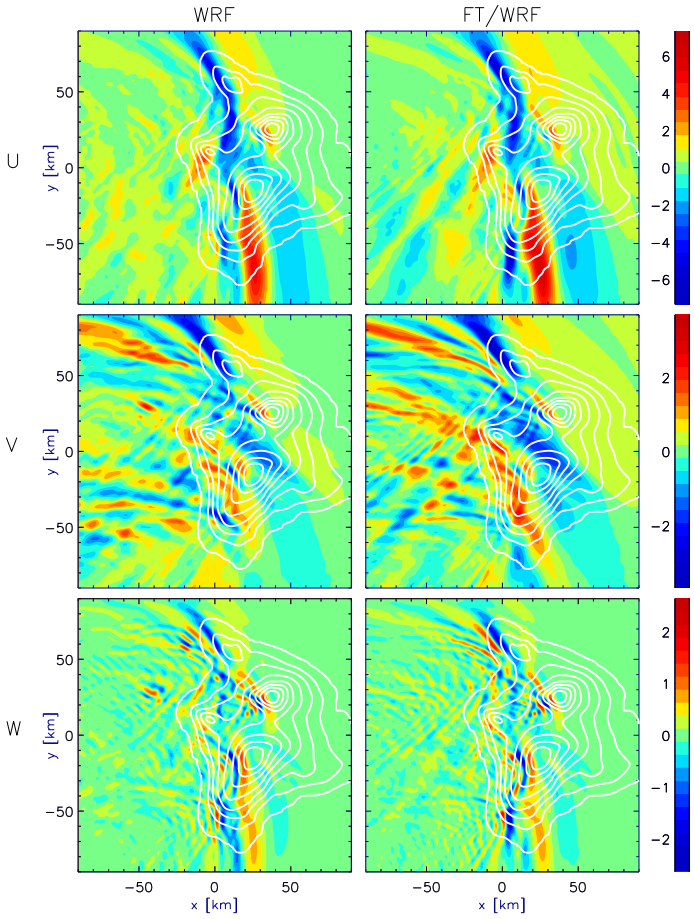

Fig. 3 Case 1. Horizontal cross-sections at $z = 10$ km of anomalies in (top) zonal, (middle) meridional, and (bottom) vertical velocity from WRF (left column) and WRF-initialized FT solution (right column). Color bar units are m s^{-1}. Topography contours are white (500 m intervals).

perturbation velocities u, v, and w at $z = 10$ km. The FT/WRF solutions were initialized with the WRF w field at $z_i = 6$ km and then propagated to $z = 10$ km using (2) and (3). The WRF and FT/WRF solutions are very similar, indicating that the wavefield above the FT initialization height of 6 km

is well approximated by linear steady-state propagating stationary gravity waves.

The multiscale three-dimensional topography of Hawaii can force gravity waves with a range of horizontal wavelengths. The polarization relations for internal gravity waves dictate that horizontal velocity perturbations tend to be dominated by long waves of low intrinsic frequency, whereas vertical velocity perturbations are largest for short waves of high intrinsic frequency, as is evident from inspection of Figure 3.

Figure 4 plots the FT/WRF solutions for the local vertical fluxes of horizontal wave momentum, $F_x = \rho\overline{uw}$ and $F_y = \rho\overline{vw}$, at $z = 10$ km, computed using (6) and (7), respectively. Also shown is the magnitude $(F_x^2 + F_y^2)^{1/2}$. These phase-averaged quantities are more localized and less noisy than the component velocity fields in Figure 3, and are thus easier to associate with particular topographic features.

The momentum fluxes in Figure 4 are largest near the northern and southern extremities of Hawaii. Surface flow acceleration is clearly seen in these diverted-flow regions of Figure 2. The resultant wave forcing at the northern and southern edges of Hawaii is analogous to that reported at the cross-stream extremities of elliptical obstacles by Ólafsson and Bougeault (1996) and of axisymmetric obstacles by Eckermann et al (2010) at highly nonlinear Froude numbers ($Fr \lesssim 0.3$). The response at the northern end of Hawaii is also influenced by the topography of Kohala.

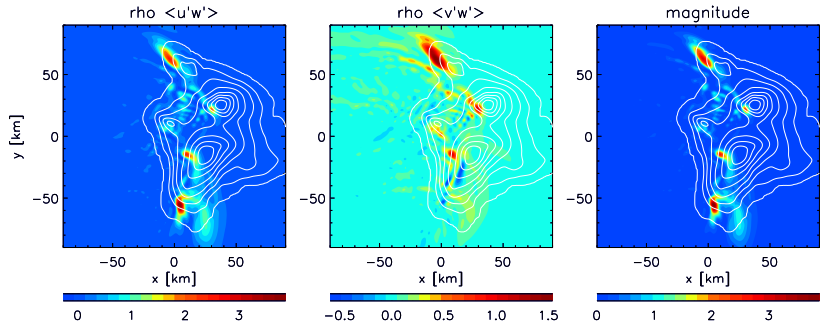

Fig. 4 Case 1. Horizontal cross-sections of locally phase-averaged momentum fluxes at $z = 10$ km from the FT/WRF method. The left panel shows $F_x = \rho\overline{uw}$, the center panel shows $F_y = \rho\overline{vw}$, and the right panel shows the magnitude $(F_x^2 + F_y^2)^{1/2}$. Color bar units are kg m^{-1} s^{-2}. The prevailing initial wind direction is from the east-northeast. Topography is overlaid with white contours (500 m intervals).

Localized flux maxima appear in Figure 4 slightly downstream of the peaks of Mauna Loa and Mauna Kea. The localization of maximum wave fluxes in a narrow zone just downstream of these peaks is in close agreement with the findings of Eckermann et al (2010) for nonlinear flow over idealized axisymmetric obstacles. It arises due to the abrupt leeside collapse and ascent of isentropes triggered by upstream flow stagnation and splitting. This leeside isentropic structure provides the dominant obstacle-like forcing of waves at these altitudes, and so the linear dividing-streamline solution based on the clipped mountain h_{ds} does not describe these wave fields and fluxes accurately (Lindeman et al, 2008; Eckermann et al, 2010). Thus, in this case, both Mauna Loa and Mauna Kea are acting much like isolated individual obstacles

to the local flow, with each generating waves due to a local nonlinear leeside fluid-dynamical responses.

The streamlines in Figure 2 show flow splitting on the upslopes to Kohala, Mauna Kea and Mauna Loa but also higher-level streamlines flowing over these peaks, consistent with the observed waves generated from these peaks. By contrast, flow in and around Hualālai in Figure 2 is inhomogenous, with a recirculating southwesterly flow to the northwest of the peak due to lee vortices from Kohala, and a northwesterly flow to the southeast of the peak due to flow splitting around Mauna Loa. This local surface flow pattern is less effective in forcing waves from Hualālai. Indeed the momentum flux magnitudes (right panel of Figure 4) show relatively small wave momentum fluxes emanating from this peak. This finding is consistent with idealized obstacle simulations, which show strong suppression of both pressure and wave drag from a second obstacle located within the downstream wake generated by flow over and around an upstream obstacle (Wells et al, 2008b).

The areally-integrated wave momentum fluxes, or wave drag components, for the FT/WRF method are

$$D_{uw} = \int\int \rho\, uw\, dxdy\,, \tag{8}$$

$$D_{vw} = \int\int \rho\, vw\, dxdy\,. \tag{9}$$

yielding $D_{uw} = 4.66 \times 10^9$ kg m s^{-2} and $D_{vw} = 1.62 \times 10^9$ kg m s^{-2} at $z = 10$ km. This net wave drag vector, due to wave flux radiated from all the terrain features, is directed almost parallel to the incident flow direction. For

the WRF model alone, the results are comparable: $D_{uw} = 3.25 \times 10^9$ kg m s^{-2} and $D_{vw} = 1.33 \times 10^9$ kg m s^{-2}.

When the FT method is initialized traditionally (linearly) using the topography $h(x, y)$, we get $D_{uw} = 5.41 \times 10^{10}$ kg m s^{-2} and $D_{vw} = 1.19 \times 10^{10}$ kg m s^{-2}, a difference of roughly an order of magnitude. This is further indication of the reduction in effective mountain height for gravity wave forcing due to low-level nonlinear processes.

Another calculation was performed where the dividing streamline approximation served as the lower boundary condition. As previously mentioned, the dividing streamline height $z_c = 3.2$ km in the cases conducted here, and we initialize using the dividing streamline topography $h_{ds}(x, y)$ at $z_i = z_c$. For this FT simulation, $D_{uw} = 7.05 \times 10^8$ kg m s^{-2} and $D_{vw} = 1.71 \times 10^8$ kg m s^{-2}, which is about an order of magnitude smaller than the FT/WRF wave drag values. Given that the two wave-flux peaks above the downslope of Mauna Loa and Mauna Kea were governed by nonlinear responses not captured by h_{ds}, and that two additional and larger flux peaks occurred due to acceleration of the flow along these diverted surface streamlines and increased surface forcing at the cross-stream extremities of Hawaii, then this large underestimation of the wave drag by dividing streamline theory is not surprising.

3.2 Case 2: Northeasterly Flow.

Here the background wind direction is from the northeast with the same speed of 8 m s^{-1} as in the previous case ($Fr = 0.2$). The resulting WRF surface

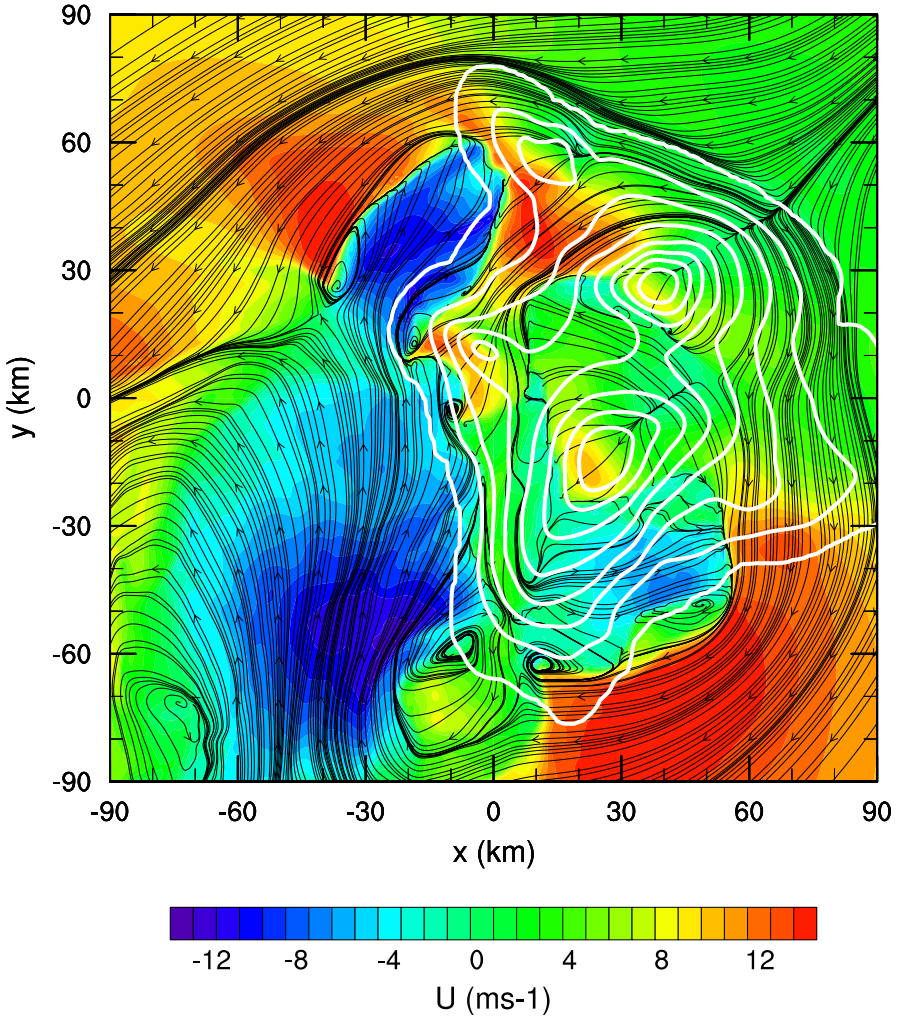

Fig. 5 As in Figure 2 but for northeasterly flow (Case 2).

streamlines are shown in Figure 5, the WRF and FT/WRF solutions at $z =$ 10 km are compared in Figure 6, and the local phase-averaged wave momentum fluxes at $z = 10$ km are shown in Figure 7. Despite the same Fr and a change in wind direction of only 22.5°, there are some large changes in the forced wave fields.

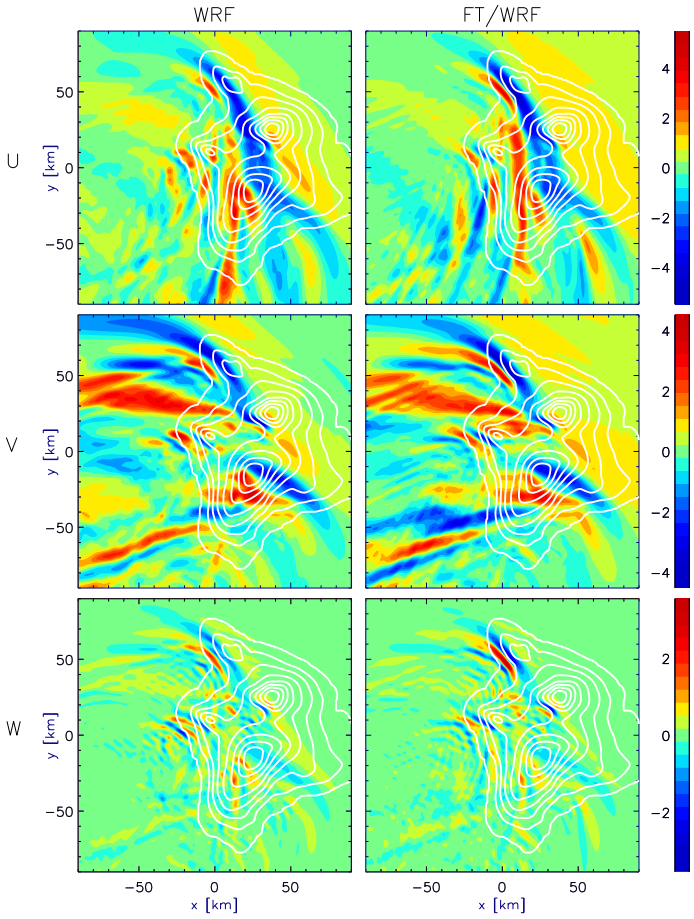

Fig. 6 Case 2. Horizontal cross-sections for u, v, and w at $z = 10$ km for northeasterly flow. WRF solutions (left column). FT/WRF solutions (right column). Color bar units are m s^{-1}. Topography is overlaid with white contours (500 m intervals).

Compared with the case of east-northeast winds, there is a substantial diminution of the momentum flux peak near the southern tip of Hawaii (c.f. Figures 4 and 7). This can be explained by comparing the low-level streamlines in Figures 2 and 5. For the east-northeasterly flow, Figure 2 shows a uniform near-easterly flow pattern over the southernmost regions of Hawaii

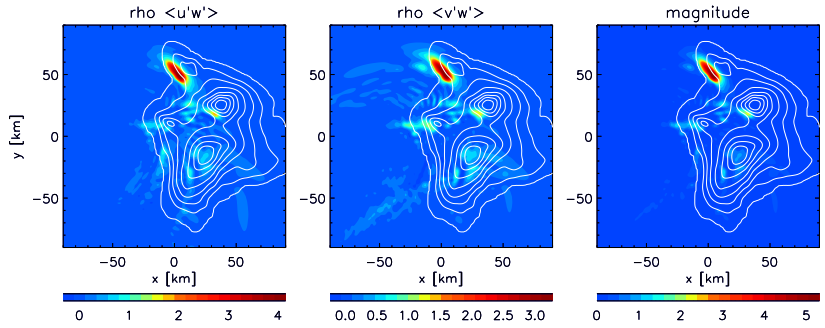

Fig. 7 As in Figure 4, but for northeasterly flow.

which forces waves. By contrast, the northeasterly flow in Figure 5 results in diverted streamlines pushed further south. Flow over the southern portions of the island is now dominated by local vortices and a recirculating westerly flow regime, which presents a weaker and more disorganized surface forcing environment that is far less conducive to wave generation and transmission to higher levels.

The momentum fluxes in Figure 7 are dominated by waves from the quasi-elliptical northern peak of Kohala, yielding northeastward wave momentum fluxes peaking in magnitude at $\sim$5.2 kg m^{-1} s^{-2}. The northeasterly flow direction is almost perpendicular to the long axis of this peak, which, if it were an isolated three-dimensional elliptical obstacle, is the optimal configuration for generating large-amplitude, less-dispersed gravity waves (Smith, 1989; Wells et al, 2008a). If we treat Kohala here as an isolated elliptical obstacle, its maximum height of $\sim$1200 m yields a local Froude number of 2/3, which should trigger a high drag wave-breaking state (Ólafsson and Bougeault, 1996). The

localization of wave flux above the lee downslope in Figure 7 is the signature of waves generated by the leeside collapse of isentropes anticipated at $Fr \sim 2/3$ (Lindeman et al, 2008; Eckermann et al, 2010), and here WRF also produces a turbulent kinetic energy (TKE) maximum in the lowest 5 km associated with low-level wave breaking (not shown). The flux peak and wavebreaking would both be expected to split into two and migrate to the cross stream extremities of Kohala if the local Fr was nearer 0.2 (Ólafsson and Bougeault, 1996), while the flux maximum would lie nearly above the obstacle peak if local Froude numbers were $\gtrsim 1$ (Eckermann et al, 2010). Thus the properties of the waves forced by Kohala can be interpreted to some extent here by treating it as if it were an isolated elliptical obstacle. Note, however, that a similar approach cannot explain the split-flow dynamics around Kohala in Figure 5. This low-level flow originates not from ocean points to the northeast of Kohala, but from regions well to the southeast due to prior flow splitting on the Mauna Kea upslope. Thus the low-level dynamics around Kohala cannot be modeled without considering the orography of the entire island.

The magnitude of the momentum flux from Mauna Kea in Figure 7 is comparable to that in the previous east-northeasterly case; however there is a significant reduction in wave momentum flux from Mauna Loa. Although the rotation of the wind from east-northeasterly to northeasterly places Mauna Loa more directly in the wake of Mauna Kea, streamline plots at $z = 3500$ m in Figure 8 reveal that the speed and direction of upstream flow impinging on the Mauna Loa peak is largely unaffected by Mauna Kea at these altitudes. The

northeasterly winds align closely with a steep topographic gradient downwind of Mauna Kea that generates a narrow region of flow stagnation and reversal in the lee in Figure 8. This flow generates waves above the lee downslope of Mauna Kea as before. By contast, the topography of Mauna Loa is slightly elliptical and it's long axis aligns with the northeasterly flow, a configuration that produces much weaker wave and lee-vortex responses in idealized obstacle simulations (Smith, 1989). Indeed, unlike Mauna Kea, the flow immediately downstream of Mauna Loa in Figure 8 shows no evidence of stagnation or reversal. This weaker dynamical response due to the coalignment of the incident flow with the long-axis of the Mauna Loa peak appears to explain the weaker wave fluxes in this case.

Near Hualālai, the surface streamlines in Figure 5 indicate a significant shift in surface wind direction from the previous east-northeasterly case, with the surface flow approaching Hualālai from the northeast and flowing over the peak. The resulting forced wave momentum flux in Figure 7 stretches out west of the peak, due to preferential generation over the steepest topographic gradients.

The integrated drag values calculated by the FT/WRF method are $D_{uw} = 3.21 \times 10^9$ kg m^{-1} s^{-2} and $D_{vw} = 3.37 \times 10^9$ kg m^{-1} s^{-2}. The values from WRF alone are $D_{uw} = 2.28 \times 10^9$ kg m^{-1} s^{-2} and $D_{vw} = 2.60 \times 10^9$ kg m^{-1} s^{-2}. Again, the net wave flux from all the peaks is directed roughly parallel to the incident flow. As in the previous case, there is an order of magnitude difference between these values and the linear FT values, which are $D_{uw} =$

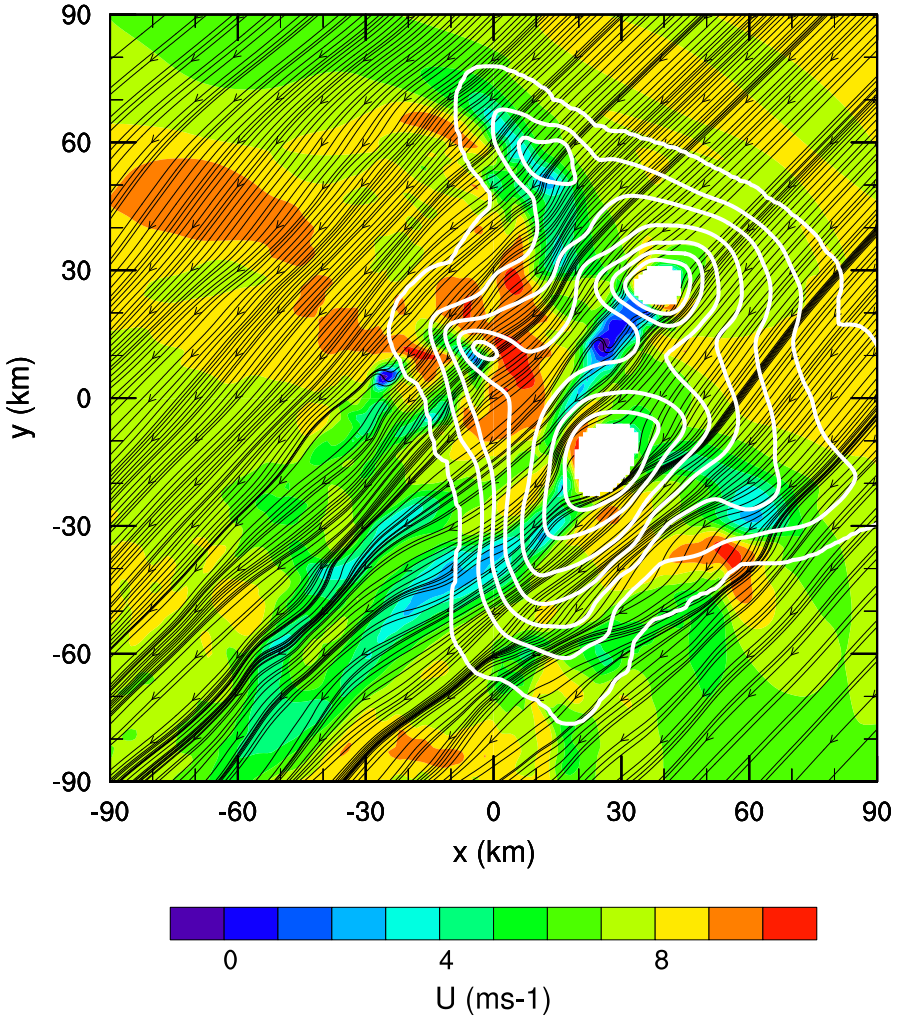

Fig. 8 Surface streamlines at $z = 3500$ m and $t_i = 12$ hours for the Case 2 WRF simulation with **U** directed northeasterly at 8 m s^{-1}. Color shading shows absolute winds along the **U** direction (see underlying color bar, units in m s^{-1}). Topography is overlayed as white contours at 500 m intervals..

3.89×10^{10} kg m^{-1} s^{-2} and $D_{vw} = 2.81 \times 10^{10}$ kg m^{-1} s^{-2}. When the dividing streamline approximation is applied, the drag magnitudes are again nearly an

order of magnitude lower than those observed: $D_{uw} = 4.88 \times 10^8$ kg m^{-1} s^{-2} and $D_{vw} = 4.44 \times 10^8$ kg m^{-1} s^{-2}.

4 Discussion and Summary

We have shown that a linear Fourier-transform mountain-wave model can be coupled to a nonlinear mesoscale model to characterize waves forced by nonlinear flow over and around the complex topography of (the Big Island of) Hawaii. The coupling was accomplished by using the mesoscale model solution for the vertical velocity to initialize the Fourier transform model at a height of 6 km. The coupling was tested by running the mesoscale model separately to 10km altitude and comparing the result with that of the coupled Fourier transform method.

A second new tool was applied to this Hawaii simulation. The perturbation velocities were converted from real to complex variables, using what is effectively a Hilbert transform. In complex form, the local phase average can be obtained. The local phase-averaged momentum fluxes calculated in this way were key to interpreting the results, since wave fluxes were concentrated in small areas usually near the individual peaks of Hawaii in Figure 1.

This particular approach to studying wave generation from Hawaii is motivated by the need to accurately parameterize the significant drag forces on the large-scale flow due to momentum flux deposition by mountain waves that are not resolved explicitly by global climate and weather models (Kim et al, 2003). Climate models typically run at horizontal resolutions for which Hawaii

would be completely contained within a single grid box. In such models, total wave drag from the island must be parameterized within that model grid box. Higher resolution weather models would divide Hawaii among a number of smaller grid boxes, which might explicitly resolve the large-scale island relief but would not adequately resolve the smaller subsidiary peaks identified in Figure 1. Thus the total wave drag and the wave drag from individual peaks are relevant to the parameterization of mountain wave drag in models.

We performed WRF simulations using representative surface flow conditions for Hawaii, namely a east-northeasterly to northeasterly trade-wind flow of $Fr = 0.2$ that produces strong flow splitting and downstream lee vortices (Smolarkiewicz et al, 1988; Rasmussen et al, 1989; Smith and Grubišić, 1993), a situation for which there are no clear predictions of the type of mountain wave activity expected at higher altitudes to aid parameterization development. Our approach shows some promise as a way of informing this difficult parameterization problem.

The major findings of this pilot study for Hawaii are as follows:

- wave momentum flux is dominated by flow over individual island peaks and surface acceleration at the cross-stream edges of the island. The large-scale island topography drives flow separation and lee vortex generation rather than wave forcing.
- individual peaks can act as quasi-axisymmetric or quasi-elliptic obstacles and generate wave momentum flux that is concentrated above the downslope through the forcing effects of leeside collapse and ascent of isentropes,

much as seen in simulations for idealized isolated obstacles (Eckermann et al, 2010).

- for east-northeasterly flow we find wave generation at the northern and southern extremities of Hawaii, consistent with the wave forcing at the cross-stream extremities of idealized obstacles at $Fr \lesssim 0.3$ noted by Ólafsson and Bougeault (1996) and Eckermann et al (2010).
- some wave features prove sensitive to a small change in wind direction from east-northeasterly to northeasterly, with wave flux over Kohala intensifying, over Mauna Loa weakening, and near the southern tip of Hawaii almost disappearing. The latter feature arises due to vortex generation in the south that reduces wave forcing. The former two features are ascribed to the sensitivity of wave responses to flow direction due to the elliptical nature of these peaks.
- despite this variability, the areally-integrated wave momentum flux (wave drag) vectors show similar magnitudes and strong alignment with the incident flow direction.
- wave drag is roughly an order of magnitude smaller than linear predictions, consistent with the strong flow splitting and lee vortex generation
- wave drag is roughly an order of magnitude larger than that predicted by a Sheppard-based dividing streamline parameterization, due to larger wave fluxes from individual peaks *via* leeside isentropic collapse, and wave forcing at the north-south island extremities by flow diversion.

A future extension of this work would be to take the Fourier solution of the wavefield to much higher altitudes through realistic background winds, for Hawaii and other locations. The advantage of using a coupled mesoscale-Fourier model instead of a mesoscale model at all altitudes is an improved ability to interpret the results and a faster computation speed with similar or better resolution. The Fourier method should be implemented with a ray-tracing formulation to handle turning points and critical layers practically (e.g., Broutman et al, 2006; Eckermann et al, 2006), and with a wavebreaking parameterization. The mesoscale-Fourier coupling would not be suitable in situations where, for example, wavebreaking or other nonlinearity aloft is strong enough to have a significant feedback effect on low-level flow and mountain-wave generation.

Acknowledgements We thank the reviewers for helpful comments. This work was supported by the National Science Foundation through grants ATM-0448888 (JL) and ATM-0435789 (DB), by NASA GMAP contract NNG06HM19I (SDE, JM, DB), and by the Office of Naval Research through the NRL base 6.1 research program (SDE).

References

Broutman D, Ma J, Eckermann SD, Lindeman J (2006) Fourier-ray modeling of transient trapped lee waves. Mon Wea Rev 143:2849–2856

Broutman D, Eckermann SD, Rottman JW (2009) Practical application of two turning-point theory to mountain-wave transmission through a wind jet. J Atmos Sci 66:481–494

Chen YL, Feng J (2001) Numerical simulations of airflow and cloud distributions over the windward side of the island of Hawaii. Part i: The effects of trade wind inversion. Mon Wea Rev 129:1117–1134

Chen YL, Nash AJ (1994) Diurnal variation of surface airflow and rainfall frequencies on the island of Hawaii. Mon Wea Rev 122:34–56

Davies LA, Brown AR (2001) Assessment of which scales of orography can be credibly resolved in a numerical model. Quart J Roy Meteor Soc 127:1225–1237

Ding L, Calhoun RA, Street RL (2003) Numerical simulation of strongly stratified flow over a three-dimensional hill. Bound-Layer Meteor 107:81–114

Eckermann SD, Broutman D, Ma J, Lindeman J (2006) Fourier-ray modeling of short wavelength trapped lee waves observed in infrared satellite imagery near Jan Mayen. Mon Wea Rev 134:2830–2848

Eckermann SD, Lindeman J, Broutman D, Ma J, Boybeyi Z (2010) Momentum fluxes of gravity waves generated by variable Froude number flow over three-dimensional obstacles. J Atmos Sci (in press), DOI 10.1175/2010JAS3375.1, URL http://journals.ametsoc.org/doi/abs/10.1175/2010JAS3375.1, http://journals.ametsoc.org/doi/abs/10.1175/2010JAS3375.1

Hafner J, Xie SP (2003) Far-field simulation of the Hawaiian wake: Sea surface temperature and orographic effects. J Atmos Sci 60:3021–3032

Hahn SL (1996) Hilbert transforms in signal processing. Artech House

Jiang Q, Doyle JD, Smith RB (2005) Blocking, descent and gravity waves: Observations and modelling of a MAP northerly föhn event. Quart J Roy

Meteor Soc 131:675–701

Kim YJ, Eckermann SD, Chun HY (2003) An overview of the past, present, and future of gravity-wave drag parameterization for numerical climate and weather prediction models. Atmos-Ocean 41:65–98

Klemp JB, Dudhia J, Hassiotis AD (2008) An upper gravity-wave absorbing layer for NWP applications. Mon Wea Rev 136:3987–4004

Lindeman J (2008) A numerical study of topographical effects on flow regimes in the lower atmosphere. PhD thesis, George Mason University

Lindeman J, Broutman D, Eckermann SD, Ma J, Rottman JW, Boybeyi Z (2008) Mesoscale model initialization of the Fourier method for mountain waves. J Atmos Sci 65:2749–2756

Miranda PMA, James IN (1992) Non-linear three-dimensional effects on gravity-wave drag: Splitting flow and breaking waves. Quart J Roy Meteor Soc 118:1057–1081

Ólafsson H, Bougeault P (1996) Nonlinear flow past an elliptic mountain ridge. J Atmos Sci 53:2465–2489

Rasmussen RM, Smolarkiewicz P, Warner J (1989) On the dynamics of Hawaiian cloud bands: comparison of model results with observations and island climatology. J Atmos Sci 46:1589–1608

Schär C, Durran DR (1997) Vortex formation and vortex shedding in continuously stratied flows past isolated topography. J Atmos Sci 54:534–554

Skamarock WC, Klemp JB, Dudhia J, Gill DO, Barker DM, Duda MG, Huang XY, Wang W, Powers JG (2008) A description of the advanced research

WRF version 3. NCAR Tech. Note NCAR/TN–475+STR, NCAR

Smith RB (1989) Mountain-induced stagnation points in hydrostatic flow. Tellus 41A:270–274

Smith RB, Grubišić V (1993) Aerial observations of Hawaii's wake. J Atmos Sci 50:3728–3750

Smith RB, Skubis S, Doyle JD, Broad AS, Kiemle C, Volkert H (2002) Mountain waves over Mont Blanc: influence of a stagnant boundary layer. J Atmos Sci 59:2073–2092

Smith RB, Doyle JD, Jiang Q, Smith SA (2007) Alpine gravity waves: Lessons from MAP regarding mountain wave generation and breaking. Quart J Roy Meteor Soc 133:917–936

Smolarkiewicz PK, Rotunno R (1989) Low Froude number flow past three-dimensional obstacles. Part i: Baroclinically generated lee vortices. J Atmos Sci 46:1154–1164

Smolarkiewicz PK, Rotunno R (1990) Low Froude number flow past three-dimensional obstacles. Part ii: Upwind flow reversal zone. J Atmos Sci 47:1498–1511

Smolarkiewicz PK, Rasmussen RM, Clark TL (1988) On the dynamics of Hawaiian cloud bands: island forcing. J Atmos Sci 45:1872–1905

Snyder WH, Thompson RS, Eskridge RE, Lawson RE, Castro IP, Lee JT, Hunt JCR, Ogawa Y (1985) The structure of strongly stratified flow over hills: dividing streamline concept. J Fluid Mech 152:249–288

Wang JJ, Juang HMH, Kodama K, Businger S, Chen YL, Partain J (1998) Application of the NCEP regional spectral model to improve mesoscale weather forecasts in Hawaii. Wea Forecasting 13:560–575

Wells H, Vosper SB, Ross AN, Brown AR, Webster S (2008a) Wind direction effects on orographic drag. Quart J Roy Meteor Soc 134:689–701

Wells H, Vosper SB, Webster S, Ross AN, Brown AR (2008b) The impact of mountain wakes on the drag exerted on downstream mountains. Quart J Roy Meteor Soc 134:667–687